Rheo-PIV of a shear-banding wormlike micellar solution under large amplitude oscillatory shear

Citation: Dimitriou, Christopher J. et al. "Rheo-PIV of a Shear-banding Wormlike Micellar Solution Under Large Amplitude Oscillatory Shear." Rheologica Acta 51.5 (2012): 395–411.

As Published: http://dx.doi.org/10.1007/s00397-012-0619-9

Publisher: Springer-Verlag

Persistent URL: http://hdl.handle.net/1721.1/79095

Version: Author's final manuscript: final author's manuscript post peer review, without publisher's formatting or copy editing

Noname manuscript No.
(will be inserted by the editor)

Rheo-PIV of a Shear-Banding Wormlike Micellar Solution under Large Amplitude Oscillatory Shear

Christopher J. Dimitriou · Laura Casanellas · Thomas J. Ober · Gareth H. McKinley

Received: date / Accepted: date

Abstract We explore the behavior of a wormlike micellar solution under both steady and large amplitude oscillatory shear (LAOS) in a cone–plate geometry through simultaneous bulk rheometry and localized velocimetric measurements. First, particle image velocimetry is used to show that the shear banded profiles observed in steady shear are in qualitative agreement with previous results for flow in the cone–plate geometry. Then under LAOS, we observe the onset of shear-banded flow in the fluid as it is progressively deformed into the non-linear regime - this onset closely coincides with the appearance of higher harmonics in the periodic stress signal measured by the rheometer. These harmonics are quantified using the higher order elastic and viscous Chebyshev coefficients e_n and v_n, which are shown to grow as the banding behavior becomes more pronounced. The high resolution of the velocimetric imaging system enables spatiotemporal variations in the structure of the banded flow to be observed in great detail. Specifically, we observe that at large strain amplitudes ($\gamma_0 \geq 1$) the fluid exhibits a 3-banded velocity profile with a high shear rate band located in-between two lower shear rate bands adjacent to each wall. This band persists over the full cycle of the oscillation, resulting in no phase lag being observed between the appearance of the band and the driving strain amplitude. In addition to the kinematic measurements of shear banding, the methods used to prevent wall slip and edge irregularities are discussed in detail, and these methods are shown to have a measurable effect on the stability boundaries of the shear banded flow.

Keywords Shear Banding · LAOS · Particle Image Velocimetry · Wall Slip · Wormlike Micelles

C. J. Dimitriou, L. Casanellas, T. J. Ober, G. H. McKinley
Hastopoulos Microfluids Laboratory
Department of Mechanical Engineering
Massachusetts Institute of Technology
Cambridge, MA, USA E-mail: gareth@mit.edu

L. Casanellas
Departament d'Estructura i Constituents de la Matèria, Facultat de Física
Universitat de Barcelona
Av. Diagonal 647 08028 Barcelona, Spain

1 Introduction

Shear banding refers broadly to the phenomenon whereby a complex fluid subjected to a simple homogenous shear deformation exhibits two or more neighboring regions of markedly differing shear rates. Numerous classes of non-Newtonian fluids are known to exhibit shear banding behavior (Olmsted, 2008), from various kinds of yield stress fluids (Møller et al, 2008; Divoux et al, 2010) to entangled polymer melts (Tapadia et al, 2006; Hu, 2010) and wormlike micellar solutions (Britton and Callaghan, 1997; Salmon et al, 2003; Manneville et al, 2004b,a; Lopez-Gonzalez et al, 2006; Boukany and Wang, 2008; Lettinga and Manneville, 2009). Wormlike micelles are a particularly interesting class of shear banding systems because they are widely used in consumer products, and they have become a canonical model system for probing shear banding. The bulk rheology of these particular systems has been studied extensively by other workers (Rehage and Hoffmann, 1991; Berret et al, 1994; Schmitt et al, 1994; Cates and Fielding, 2006; Lerouge and Berret, 2010). With recent developments in experimental techniques that can be used to directly measure deformation/velocity fields in these fluids (see the review by Manneville (2008)), there has been a growth of interest in connecting measurements of the bulk rheology and the local flow behavior in

order to better understand the phenomenon of shear banding and the coupling between kinematic changes in the flow and the resulting stress-shear rate profile. Such measurements can serve as sensitive tests of the prediction of different proposed constitutive models for shear-banding materials.

There are numerous experimental techniques that have been used to study shear banding and other types of spatial heterogeneities in steady shear flow. These include NMR velocimetry (Callaghan, 2008; Møller et al, 2008; Davies et al, 2010), in which velocity fields are extracted from the spin polarization of nuclei that interact with a strong external magnetic field gradient. Another widely used method is ultrasound velocimetry (Manneville et al, 2005; Gibaud et al, 2008), which utilizes high frequency ultrasonic pulses to produce ultrasonic speckle patterns from which velocity fields across the gap of a Couette cell can be extracted. Finally, numerous workers have used particle tracking methods (Meeker et al, 2004a,b; Tapadia et al, 2006; Fardin et al, 2009; Helgeson et al, 2009; Dimitriou et al, 2011) in order to quantify local velocity/deformation fields.

In much of the recent work that has used particle tracking methods to observe flow in shear banding fluids, experiments have been carried out in the limit of low seeding density, where individual particles are tracked in order to determine the velocity field within the fluid. This type of tracking method is called particle tracking velocimetry (PTV). When the seeding density in the fluid is higher, the displacement of local groups of particles is determined by spatial correlations rather than tracking individual particles. This method is referred to as particle image velocimetry, or PIV (Adrian, 1991, 2005). Both PTV and PIV are well suited for observing transient responses in fluid flows, due to the good temporal and spatial resolution of these methods (Manneville, 2008), and this has been exploited by some workers to study transient evolution of shear banded flows (Miller and Rothstein, 2007). Both PTV and PIV are therefore a good choice of a tool for probing shear banding in oscillatory flows, although recent developments in Rheo-NMR techniques discussed by Callaghan (2008) and Davies et al (2010) have provided spatial and temporal resolutions that rival those of PIV/PTV methods. One advantage of PIV over PTV is that it is a whole field technique, returning velocimetric data on a uniform spaced grid (Raffel et al, 2007). Vector fields obtained from PTV tend to be sparser than those obtained from PIV, and the individual vectors are located randomly throughout the imaged domain due to the randomly positioned particles in the flow (Adrian and Westerweel, 2011). This disadvantage in general makes subsequent data analysis, including computation of differential quantities such as shear rate and vorticity, more cumbersome in the case of PTV.

As far as the specific case of studying shear banding in wormlike micellar solutions is concerned, the earliest investigations studied the phenomenon using Rheo-NMR in a cone–plate geometry (Britton and Callaghan, 1997, 1999). This approach is reasonable because it is well known that when viscometric approximations hold, spatial variations in the stress in a cone–plate geometry are very small (Bird et al, 1987). Subsequent velocimetric studies have focused more often on observing banding in cylindrical Couette geometries (Salmon et al, 2003; Manneville et al, 2004a; Miller and Rothstein, 2007). These velocimetry studies have shown that there is a clear difference between the structure of the shear-banded profiles observed in the two cases. Typically a double banded profile develops in the Couette case above a critical shear rate (i.e. one low and one high shear rate band) whereas 3-banded profiles appear in the cone–plate geometry (two low shear rate bands near the upper and lower rigid plates, and a higher shear rate band at midgap). These differences arise presumably because of the curvilinear nature of the flow fields in each device - the theoretical study by Adams et al (2008) has discussed this in detail for a particular case of the Johnson-Segalman model.

In addition to studies of banding in wall-bounded Couette cells, there have also been velocimetric studies of the onset of shear banding in these fluids within pressure driven microchannel flows (Mendez-Sanchez et al, 2003; Marín-Santibáñez et al, 2006; Nghe et al, 2008; Ober et al, 2011). Although the kinematics of steady complex fluid flow in a microchannel are spatially inhomogeneous, these experiments have been useful because they can be used to probe the nonlinear rheology of the fluids at much higher shear rates than is usually possible and can probe the onset of "non-local" effects when the characteristic length scale of the geometry and of the shear band become comparable (Masselon et al, 2008, 2010).

Finally, we note that some recent studies have suggested that both wall slip (Boukany and Wang, 2008; Lettinga and Manneville, 2009; Feindel and Callaghan, 2010) and unsteady secondary flows (Fardin et al, 2009, 2010) play an important role in the shear banding behavior of wormlike micellar solutions. Motivated by these most recent results, the work in this paper is a careful reassessment of the nonlinear rheological response of a model wormlike micellar solution in a cone and plate geometry, taking recent developments concerning wall slip and secondary flow into account. To probe the progressive onset of these rheometrical limitations systematically, we use oscillatory shearing deformations of

progressively increasing amplitude. We also provide a detailed discussion of some of the experimental issues encountered when carrying out velocimetric measurements on wormlike micellar systems - including a discussion of the effect of secondary flows on PIV imaging, an experimental method used to delay the onset of wall slip, and the consequences of employing a rigid bounding surface at the edge of the cone–plate geometry to improve image quality. After accounting for these experimental difficulties, we show that the high spatial and temporal resolution of a Rheo-PIV system developed in a previous study (Dimitriou et al, 2011), enables us to observe in detail the local deformation behavior and corresponding stress evolution in a micellar solution at the onset of shear-banding under both steady and oscillatory shearing deformations.

The shear banded velocity profiles that are observed in the cone–plate device are similar to the 3-banded profiles observed by Britton and Callaghan (1997) and are shown to be well described by a sigmoidal function - this is distinctly different from the 2-banded profiles that have been observed for flow of wormlike micelle solutions in Couette cells. Large amplitude oscillatory shear (LAOS) is used to progressively deform the material deeper into the nonlinear regime and probe the onset of shear-banding behavior in the absence of substantial secondary flows and wall slip. We also use the LAOS framework developed in previous work (Cho et al, 2005; Ewoldt et al, 2008, 2010) to connect local kinematic measurements with nonlinearities in the bulk rheology, and show that the onset of shear banded velocity profiles closely coincides with the growth of nonlinearities in the bulk viscoelastic response. Similar behavior has recently been explored using some of the microstructural constitutive models that have been proposed for describing the rheology of shear banding systems (Adams and Olmsted, 2009; Zhou et al, 2010), providing an opportunity in the future for comparing experimental data with theoretical predictions.

2 Materials and Methods

2.1 Micellar Fluid - CPyCl

In this work we focus on a single canonical wormlike micellar fluid. The particular system studied is a solution consisting of 100mM cetylpyridinium chloride (CPyCl) (Alfa Aesar) and 60mM sodium salicylate (NaSal) (Alfa Aeser) in de-ionized water. The system was seeded with 0.001 wt. % Titanium Dioxide particles (average size 3 μm, density 4200 kg/m^3 from TSI Inc.) for the purpose of the PIV measurements. These small particles result in a seeding (or number) density of particles that is high enough to carry out PIV measurements, however the low volume fraction of the particles ($\phi \simeq 2 \times 10^{-5}$) means that the particles do not significantly affect the rheology of the fluid. All measurements of the rheology of the CPyCl fluid in this paper (rheometry and combined Rheo-PIV) were carried out on a TA instruments ARG2 stress controlled rheometer equipped with a 50mm diameter, 4° cone and plate geometry (quartz plate and aluminum cone) and with the temperature controlled to 25°C. This particular test fluid differs from some of the fluids used in other shear banding studies (e.g. those by Salmon et al (2003) and Lettinga and Manneville (2009)) because it is not prepared in brine and does not contain any added sodium chloride. However, an identical fluid composition (i.e. one without salt) has been used in a wide range of previous studies that have covered topics from bulk rheology (Rehage and Hoffmann, 1991), to microfluidic rheometry and steady channel flow (Ober et al, 2011) to shear banding in cone–plate geometries (Britton and Callaghan, 1997). In figure 1 we summarize the shear rheology of the fluid (measured at 25°C) and show that it is well described by a single mode Maxwell model for low frequencies $\omega \leq 1/\lambda$, for which the viscoelastic moduli G' and G'' are given by the following expressions:

$$G'(\omega) = \frac{\eta_0 \lambda \omega^2}{1 + (\lambda\omega)^2} \qquad G''(\omega) = \frac{\eta_0 \omega}{1 + (\lambda\omega)^2} \tag{1}$$

For the data in figure 1 the fitting parameters are $\lambda = 1.45$s, $\eta_0 = 39$ Pa.s and $G_0 = 27$ Pa. In addition to this, the steady shear viscosity exhibits a strong shear thinning behavior and a clear stress plateau for rates larger than ~ 0.3 s^{-1}. In figure 1, the predicted shear stress obtained by using the Cox-Merz rule is also plotted. The Cox-Merz rule is an empirical relation that predicts that the magnitude of the complex viscosity is equal to the shear viscosity at corresponding values of frequency and shear rate (Bird et al, 1987):

$$\eta(\dot{\gamma}) = |\eta^*(\omega)|\Big|_{\omega=\dot{\gamma}} \tag{2}$$

From the Cox-Merz rule and the relationship between complex modulus and complex viscosity ($\eta^* = G^*/i\omega$) a prediction of the shear stress under steady shear can be obtained from oscillatory data. As can be seen in figure 1, there is a progressive deviation of this predicted shear stress from the measured value for shear rates larger than ~ 0.3 s^{-1} - this is in agreement with the observations made in previous studies (Pipe et al, 2010). In figure 1 we also indicate the points on the flowcurve where the strain rate amplitude of each of the oscillatory tests in section 3 lies. This helps to illustrate the fact that the progressive increase in the strain

amplitude under oscillatory shear can be interpreted, at least qualitatively, as a ramping up along the flowcurve into the stress plateau region, where shear banding is expected to occur. Additional bulk rheological measurements of an identical test fluid (eg. measurements of the normal stress data N_1) are provided in a recent study by Ober et al (2011).

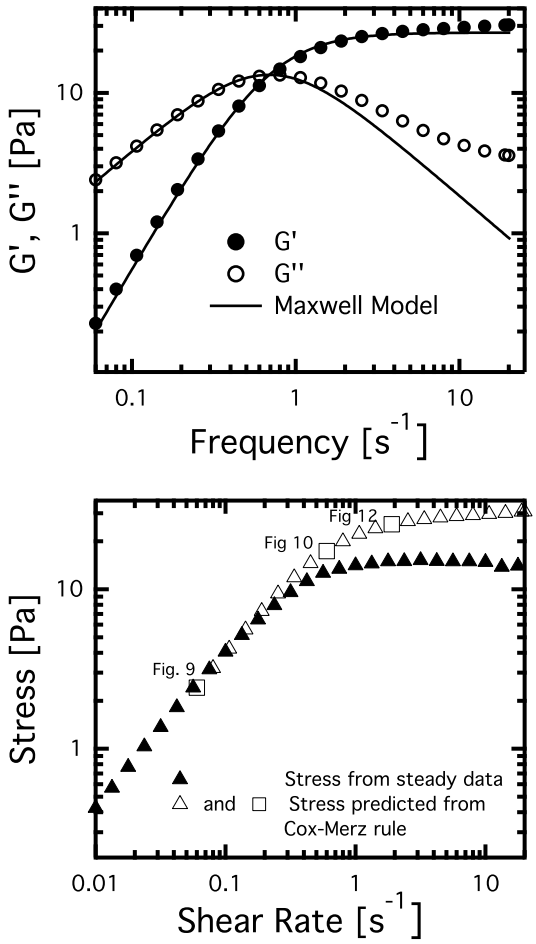

Fig. 1 Linear viscoelastic moduli of the CPyCl test fluid (top) measured at a strain amplitude $\gamma_0 = 0.1$. The data is fit to a single mode Maxwell model for low frequencies ($\omega < 2$ rad.s^{-1}), with fitting parameters $\lambda = 1.45$ s, $\eta_0 = 39$ Pa.s and $G_0 = 27$ Pa. In the lower plot, the steady flowcurve of the CPyCl system is given. The onset of pronounced shear thinning occurs around 0.3 s^{-1}. The hollow symbols correspond to the shear stress predicted from the dynamic data using the Cox-Merz rule (Bird et al, 1987). Hollow squares correspond to behavior at strain rates equal to the amplitudes used in Figures 9, 10, 12

Controlling oscillatory strain with a stress controlled rheometer One important experimental aspect of the LAOS tests done in this work is the use of a stress controlled rheometer to impose an oscillatory strain on the CPyCl test fluid. While the ARG2 can control the strain on the sample through the use of a feedback loop, for some very non-linear fluids (e.g. yield stress fluids) controlled stress instruments may fail to impose a perfectly sinusoidal deformation, resulting in higher harmonic contributions to the periodic deformation (Läuger and Stettin, 2010). For all of the present LAOS experiments, the power spectrum of the raw displacement signal from the ARG2 rheometer $\gamma(t)$ was analyzed to determine the relative magnitude of the next highest harmonic contribution to the strain field. For these experiments, the strength of the second highest harmonic contribution ($\omega_3 = 3\omega_1$) was at least 5 orders of magnitude lower than the primary forcing frequency even during shear banding. Figures are provided in the supporting information that illustrate this.

2.2 Rheo–PIV Apparatus

In order to directly observe the local strain and strain rate within the fluid under steady and dynamic shearing conditions, an experimental Rheo–PIV apparatus that mounts to an ARG2 stress controlled rheometer was designed and fabricated. The apparatus is the same as that used in a previous study of model waxy crude oils (Dimitriou et al, 2011) and is similar to experimental designs used by other workers that implement particle tracking techniques to observe shear banding and wall slip in rheometers (Meeker et al, 2004a; Tapadia et al, 2006). Two schematic diagrams of the Rheo–PIV system are shown in figure 2. This system consists of a laser light sheet which is directed downward into the sample. The sample is loaded into a cone and plate geometry, with the upper plate being a transparent quartz plate (radius $R = 25$ mm), and the lower geometry being a precision machined black anodized aluminum cone ($R = 25$ mm radius $\Theta_0 = 4°$ angle). A CCD camera (MatrixVision BlueFox) fitted with a macroscopic imaging zoom lens (Edmund Optics Techspec VZM 600i) is positioned such that the imaging plane coincides with the location of the laser light sheet. The light sheet is aligned tangentially to the direction of flow of the fluid, and approximately 2 mm into the fluid from the edge of the geometry. For a spherical (r, θ, ϕ) coordinate system oriented with its center at the cone tip and the lower cone surface being described by $\theta = \pi/2 - \Theta_0$ (and flow only occurring in the ϕ direction), this corresponds to a laser light sheet tangent to the sphere at $r = R_i = 23$ mm. The laser light sheet illuminates seed particles at different positions along the vertical (shear) direction ($y \simeq R_i(\theta - \pi/2 + \Theta_0)$), so by observing the movement of these particles in the flow

direction ϕ (or $x \simeq R_i\phi$) it is possible to determine the tangential velocity profile within the fluid.

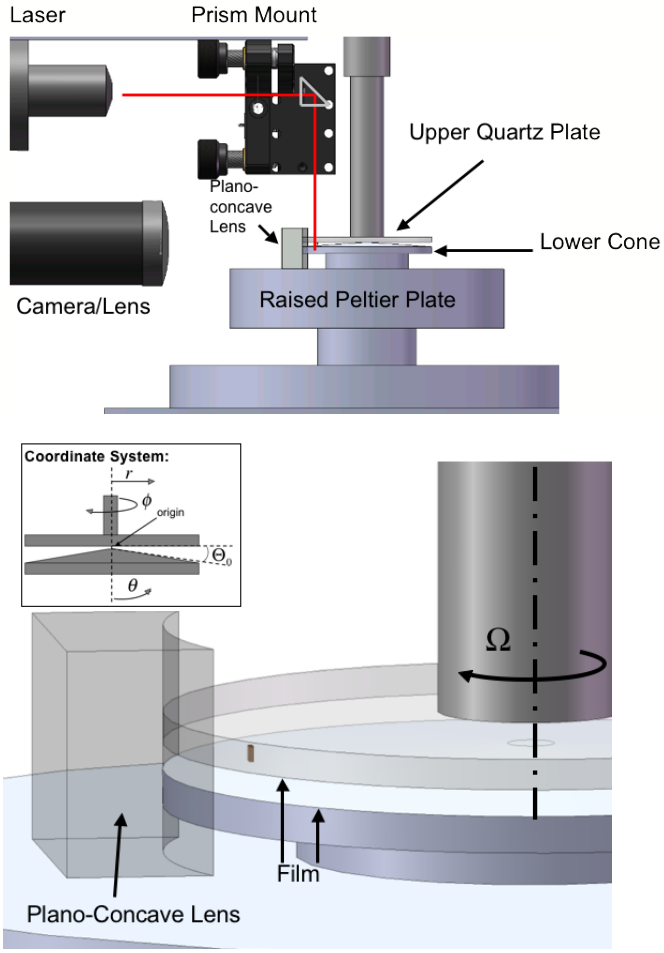

Fig. 2 Schematic diagram (top) of the Rheo–PIV system. 3D Model (bottom) showing how a plano concave lens can be placed up against the edge of the cone and plate geometry, in addition to how the transparent film is placed on the upper plate and lower cone. The coordinate system used in discussions is annotated in the box.

The velocity field within the fluid is determined using digital PIV, whereby a cross correlation algorithm is applied to a pair of images separated by a time $\frac{1}{F}$, where F is the frame rate that the CCD camera acquires images at (for our system $F = 60$ fps typically). The two subsequent images are divided into interrogation windows of size 16×16 pixels, and the 2D cross correlation function between the two successive frames in each interrogation window is computed. The point at which the cross correlation function is a maximum corresponds to the average displacement of fluid elements within the interrogation window between the two exposures. The 2D velocity field is formed from the ensemble of these displacements obtained from each interrogation window. Because the lateral width of the laser light sheet ($\Delta x \sim 2$ mm) and its thickness (~ 0.25 mm) are both small compared to the value of R_i, the flow can be assumed to be translationally invariant along the x direction. This approximation essentially takes a small enough arc segment on the surface of a sphere (and any movement of particles on this surface) and describes it using a rectangular coordinate system (x, y) with $x \simeq R_i\phi$ and $y \simeq R_i(\theta - \pi/2 + \Theta_0)$. The resulting time resolved velocity field is thus a full two dimensional vector field of the form $\bar{v} = [v_x(x, y), v_y(x, y)]$. Combined with the fact that there is, on average, no flow in the y direction (discussed in detail in section 3.2), this allows for each 2D velocity field to be averaged along the direction of flow to produce a single velocity profile per image pair, $v_x(y)$.

In this work, two optional features of the Rheo–PIV system that are used to facilitate the measurement of the local velocity field within the CPyCl system will be discussed extensively. The first is the use of a removable plano-concave lens with radius $R = 25$ mm which can be placed up against the edge of the cone and plate geometry, as shown in the bottom image of figure 2. The purpose of this lens is to provide a planar outer-facing surface through which the camera can image the field of view containing the illuminated seed particles. A flat front face prevents distortion of the image of the seed particles under flow, because rays reflected from the seed particles towards the CCD camera travel through the air-solid and solid-liquid interface at a direction normal to these interfaces. When the surface is not flat, refraction of the optical rays due to differences in the indices of refraction of the different media result in a distortion of the apparent location of the seed particles (thus making it difficult to determine the actual velocity profile within the fluid). When measuring local velocity fields within a Newtonian fluid, this plano-concave lens is typically not required. The upper and lower geometries have the same diameter, resulting in a pinning of the meniscus at the top and bottom edges and an almost flat meniscus profile. However, it is well known that viscoelastic fluids that exhibit shear banding are also likely to exhibit edge instabilities, which will result in an irregularly shaped meniscus even when it is pinned at the upper and lower edges (Keentok and Xue, 1999; Inn et al, 2005; Sui and McKenna, 2007). Previous workers have recognized this and used circular bounding films to prevent these edge irregularities (Tapadia et al, 2006). However, the effects of such bounding films can markedly change the local material response (Sui and McKenna, 2007) and should therefore be avoided if possible. The plano-concave lens used in this work serves a similar purpose to a circular bounding film,

but it does not surround the entire sample. This has the effect of lowering the incremental frictional torque that is imposed on the rotating fixture by such a surface. Nonetheless, there is still a measurable additional frictional force that is present when this lens is in place, due to the change in boundary conditions at the edge of the geometry and possible secondary flows induced near the rigid wall. This additional frictional force registers as an increase in the shear stress by approximately a factor of 2, as measured by the rheometer for the CPyCl/NaSal system at a particular shear rate. Figure 3 compares the flow curves for the fluid with, and without, the lens in place. The decrease in the shear stress for the final data point when the lens is in place is a result of the fluid being ejected from the gap, which is delayed to higher shear rates when the lens is not in place.

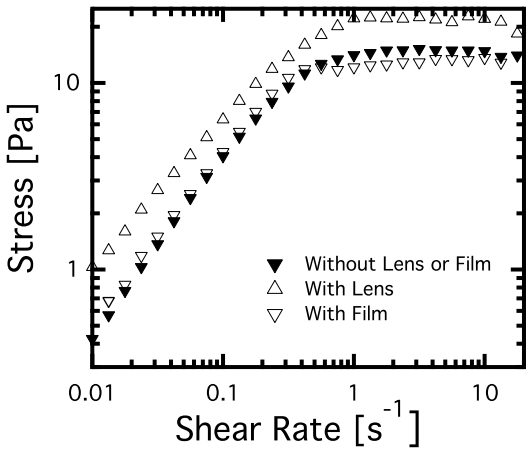

Fig. 3 Comparison of the flowcurve of the CPyCl system measured using different configurations. Filled symbols are without the lens or film. Hollow symbols are either with the lens, or with the film, but not both. The presence of the lens results in an additional frictional torque being applied to the rotating quartz geometry, which leads to an increase in the apparent shear stress measured by the instrument.

The second feature of the Rheo–PIV system that is used extensively in this work is a transparent adhesive polymer film (SS-45 screen protector manufactured by Vivitar) which can be placed on either (or both) the upper or lower geometry, such that the fluid is in contact with this film instead of the polished quartz upper plate or the machined aluminum lower conical fixture. When affixed to the upper quartz geometry, the film has the effect of increasing the roughness of the upper surface, as well as making the surface slightly more hydrophobic. Table 1 compares the contact angle of a sessile drop of CPyCl on the quartz surface with and without the adhesive plastic film, as well as the measured surface roughness. As we show below, a result of this modified surface is that slip effects which are often observed for CPyCl solutions at high shear rates (such as those seen by Lettinga and Manneville (2009)) can be suppressed to a substantial degree. The effect of surface roughness and hydrophobicity on inhibition of slip is not surprising, and these effects have been documented in previous studies (Masselon et al, 2010). Unlike the lens, this film does not have a considerable effect on the flowcurve shown in figure 3.

Table 1 Comparison of surface roughness and equilibrium contact angle of CPyCl test fluid for the aluminum cone and the quartz plate with, and without the transparent adhesive film. The roughness is measured using a Mitutoyo Surftest SJ-210 profilometer and the contact angle is measured with a Ramé Hart Model 590 contact angle goniometer. Surface roughness measures are R_a (arithmetic average of roughness values), R_q (root mean squared roughness) and R_z (maximum roughness).

Material	Aluminum Cone	Quartz Plate	Quartz + Film
Roughness			
R_a (μm)	0.28±0.04	0.014±0.001	0.045±0.007
R_q (μm)	0.35±0.06	0.018±0.001	0.067±0.01
R_z (μm)	1.8±0.5	0.115±0.006	0.5±0.09
Contact Angle	42±3°	27.3±1.4°	43±3°

Figure 4 (a) presents data from calibration experiments which demonstrate the linearity of the velocity profiles obtained by the Rheo–PIV system over a wide range of shear rates spanning those used in this work, for a Newtonian fluid (seeded heavy mineral oil with a viscosity of 0.1 Pa.s and a density of 880 kg/m^3). The velocity profiles are averaged over approximately 450 frames of video (i.e. 7.5 seconds of flow) and plotted in the form of y/H vs v/V_m, where y is the position across the gap, $H \simeq R_i\Theta_0$ is the gap height at the position $r = R_i$ ($H = 1.6$ mm) and V_m is the velocity of the top surface given by $V_m = \Omega R_i = \dot{\gamma}H$. In addition to this, Figure 4 (b) shows a comparison of the velocity profile measured for a Newtonian fluid undergoing a shear rate of $\dot{\gamma} = \Omega/\Theta_0 = 0.5$ s^{-1} when the upper and lower geometries are either covered with the adhesive film or left uncovered. As expected, the presence of the film does not alter the velocity profile. The inset in figure 4 (b) gives the probability distribution of the individual measured velocity values at a height of 0.75 mm from the lower cone. The standard deviation of the velocity measured at that location is 0.02 mm/s, which is approximately 5% of the measured velocity (determined from $\sim$ 14000 PIV correlation measurements). The experimental velocity measurements at a fixed spatial position show a well-defined average velocity with a Gaussian distribution that arises pri-

marily from small mechanical vibrations in the frame which holds the camera/lens assembly. This results in small random and uncorrelated relative displacements of the camera and rheometer, which are interpreted as small nonzero velocities in the flow by the PIV analysis (and these velocities are determined to be on the order of 0.02 mm/s, as given by the measurement of the standard deviation). However, averaging flow profiles over several frames (typically 5 or more) removes any small instantaneous bias that may result from the vibrations. While these vibrations do not have an effect on the time averaged velocity profiles, we can still see some small systematic deviations (less than 5% of V_m) of the time averaged velocity profile from the predicted linear velocity profile in figure 4 (b). These deviations are chiefly a result of the air-fluid interface at the outer sample edge which is not perfectly flat. Despite the fact that the interface is pinned at the upper and lower plates, small variations in sample volume always result in a slightly curved air-fluid interface. While these slight variations in sample volume are impossible to eliminate entirely, inspecting the shape of the interface by eye is typically sufficient to ensure that reliable velocity profiles are obtained by the Rheo-PIV apparatus.

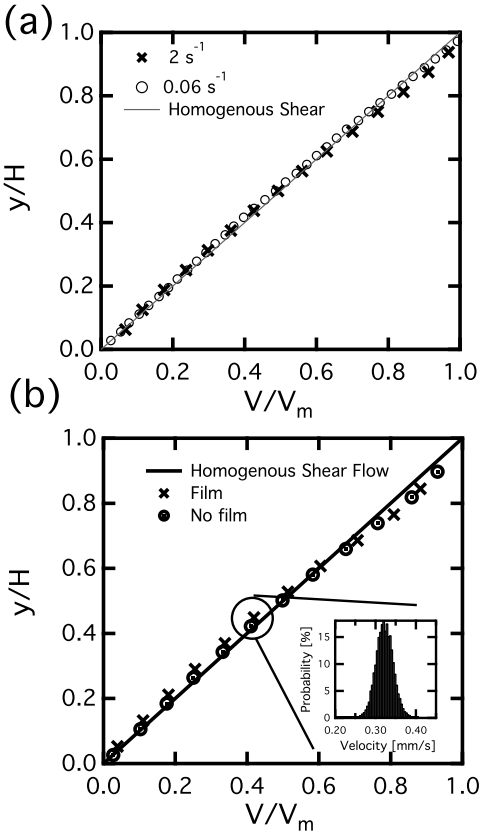

Fig. 4 Scaled velocity profile of a viscous Newtonian fluid undergoing steady shear at two different shear rates in (a), indicating linearity of the profiles. In (b), the velocity profile within the same Newtonian fluid at a fixed shear rate ($\dot{\gamma} = 0.5$ s^{-1}) is compared with the same experiment when the upper and lower plates are covered with the transparent adhesive film. The inset in (b) shows the probability distribution of the measured velocity values at a height of 0.75 mm from the lower cone.

3 Results

3.1 Steady Shear Rate banding of CPyCl

It is well known that wormlike micellar solutions exhibit shear banding under steady shear flow. Many workers have observed this behavior directly using a variety of velocimetric techniques and under a number of different flow configurations (Lettinga and Manneville, 2009; Salmon et al, 2003; Lopez-Gonzalez et al, 2006; Britton and Callaghan, 1997; Callaghan, 2008; Boukany and Wang, 2008). Britton and Callaghan (1997, 1999) showed, using NMR velocimetry, that a CPyCl:NaSal 100:60 mM system (identical to the one used in this work) exhibited a three-banded velocity profile, in which a high shear rate band is observed in the middle of the gap, connected to two lower shear rate regions near the upper and lower surfaces. Due to the fact that Britton and Callaghan (1997, 1999) worked with a fluid identical to that dealt with in this work (with similar values of the measured relaxation time and critical shear rate), and a similar flow configuration (4°/24 mm diameter and 7°/16 mm diameter ceramic cones and plates with an outer containment jacket at the edge), we expect that the velocity profiles observed here should be similar to those observed by Britton and Callaghan. Figure 5 shows the velocity field within the CPyCl solution observed using the Rheo-PIV system at a number of different imposed shear rates. As the figure shows, the velocity profiles evolve from a linear response to 3-banded profiles as the shear rate is incremented slowly from 0.1 s^{-1} to 0.75 s^{-1} and into the stress plateau region. The 3-banded profile in figure 5 at a shear rate of 0.75s^{-1} is characterized by a high shear rate region near the middle of the gap, and lower shear rate regions near the upper and lower surfaces. The behavior at the high shear rates is thus consistent with the 3-banded profiles observed by Britton and Callaghan (1997, 1999). However, Britton and Callaghan generally measured their shear banded profiles at even higher shear rates well into the stress plateau region (their use of an outer containment jacket enabled this by preventing sample from being ejected from the gap). They therefore did not probe the behavior of the fluid in this transition region

at lower shear rates. During the transition from linear to 3-banded profiles (for imposed shear rates of $\dot{\gamma} = 0.3$ s^{-1} and $\dot{\gamma} = 0.45$ s^{-1}) the material exhibits an intermediate behavior in which the flow profile appears to have two developing shear bands instead of three clearly distinct bands. This is in contrast to some shear banding scenarios which have been observed in other geometries (such as those observed by Salmon et al (2003) in Couette flow) where the shear rate in the highly sheared band remains constant and the interface between the low and high shear rate regions moves as the apparent shear rate is increased.

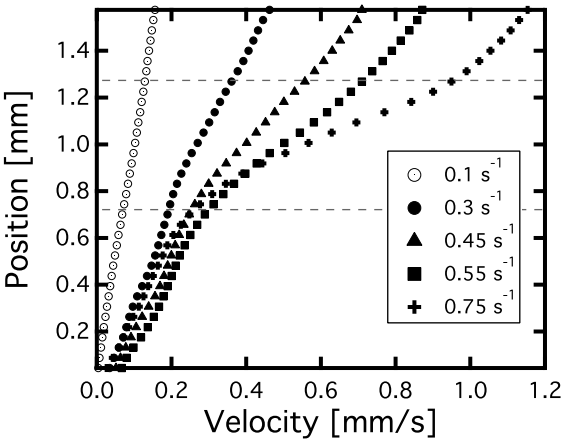

Fig. 5 Series of steady state velocity profiles observed in the CPyCl test fluid as the shear rate is incrementally changed from 0.1 s^{-1} to 0.75 s^{-1}. At the lowest shear rate the profile is clearly linear, but develops into a 3-banded profile with a region experiencing a higher shear rate near the center of the gap. The dashed grey lines indicate the location of this high shear rate region.

The data presented in Figure 5 was obtained without the plano-concave lens in place, and with the upper and lower geometries being covered by the transparent film. The transparent film was used because it was observed that it generally prevents slip from occurring at the upper, rotating plate at moderate shear rates. Figure 6 shows a comparison of the velocity profiles observed in the CPyCl system at the identical steady shear rate of 0.75 s^{-1} in the 4° cone and plate geometry with and without the use of the lens and film.

Figure 6 demonstrates the exquisite sensitivity of Rheo-PIV observations to the imposed boundary conditions. The measured velocity profiles are different in all four cases; The profiles (c-d) show that when the lens is not used, the additional presence of the film on the upper plate prevents wall slip from occurring at the upper moving surface. The presence of this wall slip results in a lower shear rate within the bulk of the fluid,

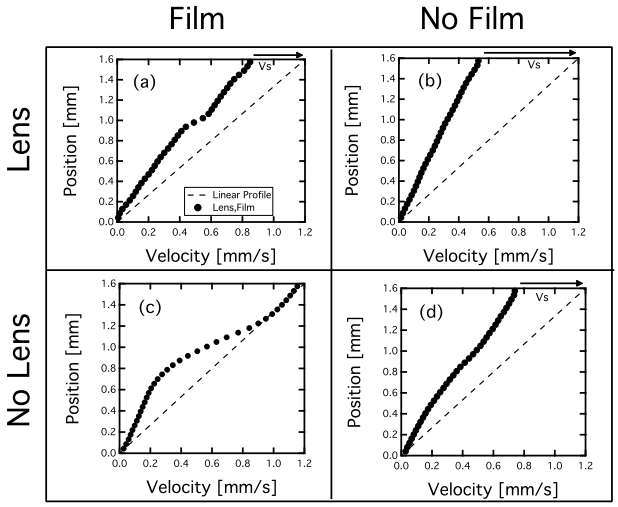

Fig. 6 Steady state velocity profiles measured at $\dot{\gamma} = 0.75$ s^{-1} under different configurations of the Rheo–PIV system. When the plano-concave lens is not used, the film clearly eliminates slip at this shear rate. When the lens is used, the film is less effective and the banded behavior exhibited by the fluid is different - a narrower band appears near the midgap.

causing the velocity profile to appear similar to the profiles observed in Figure 5 for shear rates lower than 0.75 s^{-1}. This suggests that when the plano-concave lens is not used, the transparent film eliminates wall slip and facilitates the formation of the centrally located high shear rate band. However, when the lens is used, as in (a-b), a rather different behavior is observed. Now, the addition of the transparent film only reduces the degree of slip that is present, and does not completely eliminate it. In addition to this, the appearance of the shear banded velocity profile for the case when the lens is used (figure 6 (a)) is now markedly different to the banded profile shown in figure 5 for $\dot{\gamma} = 0.75$ s^{-1}. The banded profile is now characterized by a highly localized high shear rate band in the center (only 2 or 3 data points in width) which more closely resembles a discontinuity in the velocity, as opposed to the more gradual variation in the shear rate across the gap that is observed in figure 5. In general, these narrow bands, resembling discontinuities in the velocity profile, have only been observed when the plano-concave lens is used as a bounding surface. However, we have found this behavior to be erratic and difficult to predict - the bands can be observed in different positions across the gap for the same imposed shear rates, and in other instances a larger degree of wall slip may occur on the upper surface resulting in a less pronounced high shear rate band. Two high shear rate bands have also been observed at some of the larger shear rates. One possible explanation for this irreproducible behavior is that the presence of the lens may result in an earlier onset of secondary flow

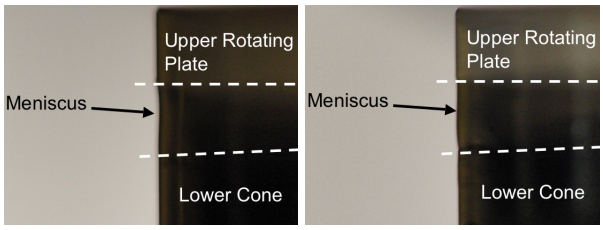

Fig. 7 Photographic image of fluid meniscus for CPyCl undergoing a shear rate of $\dot{\gamma} = 0.1$ s^{-1} (left) and $\dot{\gamma} = 0.75$ s^{-1} (right). In both cases, the meniscus remains flat and unperturbed.

within the region of the fluid near the lens, due to the altered boundary condition at the bounding surface.

In order to avoid any potential artifacts that may arise from this plano-concave lens, and also in order to avoid artifacts in our bulk rheological data (figure 3), we henceforth utilize the configuration shown in figure 6 (c) for the rest of our experimental data, i.e. an adhesive film attached to both upper and lower fixures and no lens at the outer edge. This results in reproducible and self consistent behavior as shown in figure 5. Furthermore, in figure 7 we show that at the range of shear rates probed in figure 5, no irregularities in the fluid meniscus at the edge of the cone-plate geometry are observed. This shows that a plano-concave lens or any other bounding film is in fact not required in this CPyCl fluid for velocimetric measurements at these shear rates.

3.2 Onset of Secondary Flow

The velocimetric data presented in figures 5 and 6 are only given for shear rates as high as 0.75 s^{-1}. At much larger shear rates, the local shear banded behavior of the fluid becomes much more difficult to observe for several reasons. Firstly, the likelihood of a severe edge irregularity in the meniscus arising is much greater. As described in section 2.2, this results in larger errors in the measured velocity values. While the use of the plano-concave lens (or any other type of bounding film) to impose a planar imaging surface may avoid the issue of these edge irregularities, it still affects the bulk measured stress (figure 3) as well as the flow kinematics by altering boundary conditions near the edge resulting in the erratic behavior that was discussed in section 3.1. Another difficulty that is faced at very large shear rates (typically exceeding 3 s^{-1}, or Weissenberg numbers $\mathrm{Wi} \stackrel{\mathrm{def}}{=} \lambda\dot{\gamma} \geq 4.4$) is that at the given magnification of the camera/lens, the displacement of seed particles between frames becomes sufficiently large such that the cross-correlation algorithm is unable to resolve the displacement value. This may be avoided by using a lower lens magnification, however lower magnifications result in a concomitant loss of spatial resolution for the velocity profiles. As a result of these difficulties, we choose to restrict our regime of study of the CPyCl solution to shear rates generally lower than 2 s^{-1} (or $\mathrm{Wi} \leq 2.9$), where secondary flows are less likely to occur and experimental artifacts will not play an important role in our measurements (particularly for the LAOS experiments which follow in section 3.4).

To verify that there are not any appreciable secondary flows at these lower shear rates, we used an alternative imaging method to observe flow of the CPyCl solution under steady shear in the cone–plate geometry. Specifically, a small amount of Kalliroscope AQ-RF rheoscopic fluid (http://www.kalliroscope.com/) was added to the micellar solution. This rheoscopic fluid contains a high concentration of plate–like mica seed particles. Flow alignment of these seed particles allows for macroscopic flow in the CPyCl solution to be visualized and for qualitative changes with increasing shear rate to be observed. These seed particles have been used previously to observe secondary flows in other viscoelastic fluids (McKinley et al, 1995; Fardin et al, 2009). The sample is placed in the cone–plate geometry (with upper transparent quartz plate) and illuminated from above using a white light source. A black anodized lower cone is utilized to enhance contrast of the seed particles and a camera with a telecentric zoom lens is used to observe the evolution of flow induced structures in the fluid. Figure 8 shows two images obtained from the imaging system during steady shear of the CPyCl solution at two different shear rates. At the low shear rate (2 s^{-1}) the fluid appears homogenous with no patterns emerging during the purely tangential flow. However at the higher shear rate (5 s^{-1}) radial and tangential striations in the flow field are clearly seen, as evidenced by the regions of varying contrast in the fluid further away from the center. By observing the evolution of these structures during start-up of steady shear at these higher shear rates, it is apparent that the regions of varying contrast begin to form near the rim of the sample, grow in time and propagate radially towards the center. Corresponding measurements of the total torque exerted on the fixture show the growth of temporal fluctuations (Yesilata et al, 2006; Pipe et al, 2010). This suggests that a three-dimensional unsteady secondary flow first develops near the outer edge where the sample meniscus is located, and propagates towards the center. The images in figure 8 are not intended to provide quantitative detail about the exact nature of the viscoelastic secondary flow that develops in this micellar fluid (i.e. direction, magnitude), however they do show which regions of the fluid are first afflicted, and can be used as a

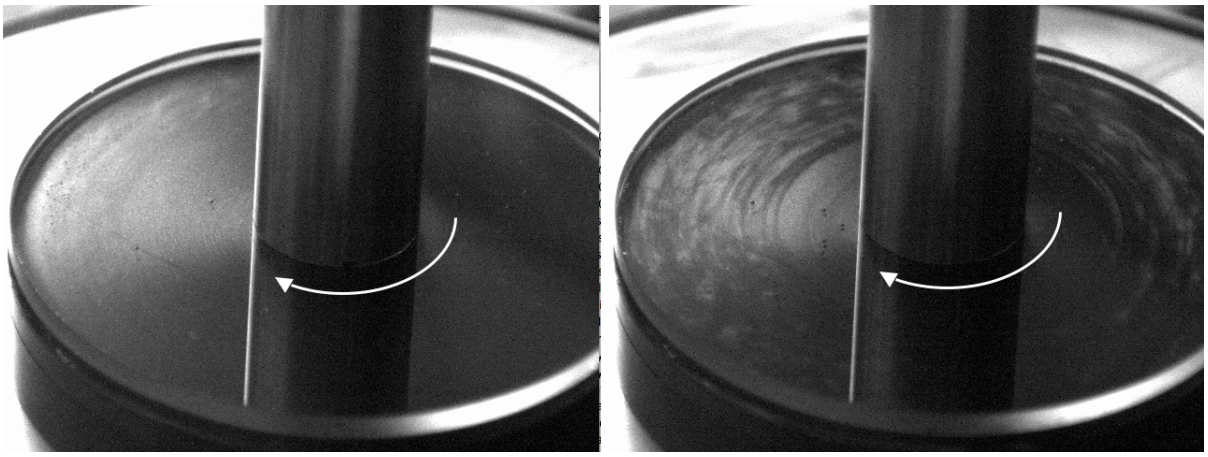

Fig. 8 Images taken during steady shear at $\dot{\gamma} = 2\ \mathrm{s}^{-1}$ (with Reynolds number $\mathrm{Re} \equiv \rho\dot{\gamma}R_i^2\Theta_0^2/\eta = 0.001$, and Weissenberg number $\mathrm{Wi} = 2.9$) on the left, and $\dot{\gamma} = 5\ \mathrm{s}^{-1}$ ($\mathrm{Re} = 0.006$, $\mathrm{Wi} = 7.3$) on the right. The distortions seen near the outer edge for the higher shear rate case are a result of the onset of secondary flow. The distortions begin appearing near the outer edge at a critical Weissenberg number $\mathrm{Wi} \simeq 6$, and grow towards the center over time. The timescale for the distortions to fill the gap is much greater than the relaxation time λ.

guideline to understand at what shear rates one might expect 2D velocimetric data from Rheo-PIV to begin to show artifacts that arise from significant viscoelastic secondary flow. Videos showing the start–up of steady shear from which the images in figure 8 are taken are provided in the supporting materials.

3.3 The Linear Viscoelastic Regime - SAOS

The ability of the Rheo–PIV setup to provide time resolved images of the local flow behavior makes it well suited for studying the behavior of complex fluids under oscillatory flow. Combined measurements of the bulk rheology and local velocity field within the CPyCl solution were therefore first obtained for small amplitude oscillatory deformations and moderate frequencies to ensure that the expected linear behavior of the fluid is recovered. For this particular experiment, the fluid is loaded into the 4° cone and plate geometry (covered with the transparent film, without the lens in place) and an oscillatory strain $\gamma = \gamma_0 \sin\omega_d t$ is imposed on the sample with $\omega_d = 0.63$ rad.s^{-1} and $\gamma_0 = 0.1$. The resulting Deborah and Weissenberg numbers for this experiment are $\mathrm{De} \equiv \lambda\omega_d = 0.91$ and $\mathrm{Wi} \equiv \lambda\omega_d\gamma_0 = 0.09$. The imaging system was set up to record images at a frame rate of $F = 60$ frames per second. At this particular frame rate, the system is able to resolve a velocity profile within the fluid every 0.017 seconds - allowing for approximately 600 velocity measurements to be made within each period of oscillation, and providing sufficient data to resolve temporal changes in the velocity field within the fluid. In figure 9 we show the combined bulk rheology (stress and strain determined from torque and angular velocity of the instrument) as well as the locally measured velocity within the fluid. In figure 9 (a) a series of velocity profiles are plotted over the course of one half period. Each velocity profile is averaged over 20 frames (both spatially for each frame, in the direction of flow, and temporally by averaging over the 20 individual frames) and plotted every 20 frames (corresponding to a 0.33 second interval). This makes individual profiles more easily discernible and minimizes random fluctuations due to small mechanical vibrations in the system. The variation in velocity across the gap is clearly linear, with no slip occurring at the bottom surface. In figure 9 (b) a comparison of the velocity of the top plate determined using two different methods is shown. The continuous line corresponds to the angular velocity of the rotating fixture $V_{\mathrm{plate}} = \omega_d R_i \cos\omega_d t$ imposed by the rheometer. The individual points (crosshairs) are data that correspond to the velocity measured in the fluid (using the PIV system) in the row of 16×16 correlation windows closest to the top plate. The comparison shows that these two velocities agree over the course of one full period of oscillation, indicating that there is no wall slip occurring at the upper surface.

The third plot shown in figure 9 (c) is a Lissajous curve of the bulk stress–strain response of the fluid to the oscillatory deformation (averaged over five periods of oscillation). The data is analyzed using the MITlaos software package (Ewoldt et al, 2008) in order to extract the decomposed elastic stress (Cho et al, 2005; Ewoldt et al, 2008) as well as the higher order Fourier/Chebyschev coefficients that describe the periodic stress response. Ewoldt et al (2008) showed how the higher order Fourier coefficients can be directly related to more physically meaningful elastic Chebyshev

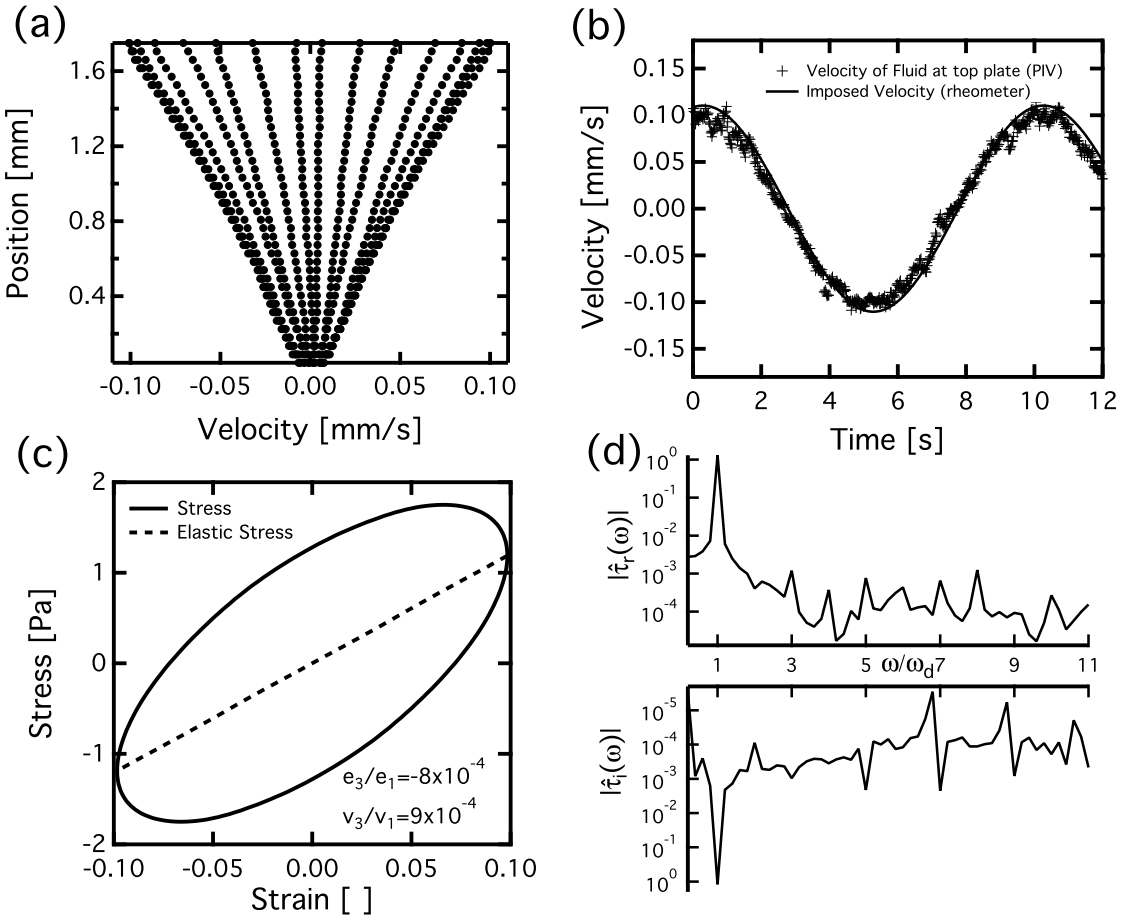

Fig. 9 Local and global rheological response of the CPyCl fluid under oscillatory shear with $\gamma_0 = 0.1$ and $\omega_d = 0.63$ rad.s^{-1} (De = 0.91, Wi = 0.09). In (a), the evolution of the local velocity field is shown over one half of a period with 15 velocity profiles evenly spaced every 0.33 seconds. In (b) the velocity of the fluid at the top plate (determined using PIV) is compared with the imposed velocity of the upper rotating surface - their close agreement indicates no slip is occuring. In (c) the bulk stress and strain are plotted in the form of a Lissajous curve, and in (d) the power spectrum of the stress is provided by plotting the real and imaginary parts of the discrete Fourier transform of the stress, $\hat{\tau}(\omega)$.

coefficients e_n and viscous Chebyshev coefficients v_n. By computing the magnitude of the ratio of the third order coefficients to the first order coefficients (e_3/e_1 and v_3/v_1) it is possible to determine the extent of nonlinearity in the material response. From the low values $e_3/e_1 = -8 \times 10^{-4}$ and $v_3/v_1 = 9 \times 10^{-4}$ and the ellipsoidal nature of the Lissajous curve it is clear that the material is exhibiting primarily a linear response at this strain amplitude and frequency. Additional details pertaining to the higher-harmonics of the stress response are provided in the form of a power spectrum in figure 9 (d). The power spectrum is illustrated by plotting the magnitude of both the imaginary and real parts of the Fourier transform $\hat{\tau}(\omega)$ of the stress response $\tau(t)$ against the frequency index ω/ω_d (where $\omega_d = 0.63$ s^{-1} is the driving frequency). The imaginary part of the Fourier transform $\hat{\tau}_i(\omega)$ corresponds to the component of the stress which is in-phase with the strain $\gamma = \gamma_0 \sin \omega_d t$ and the magnitude of the local peaks $\hat{\tau}_i(n\omega_d)$ are directly related to the elastic Chebyshev coefficients e_n (see Ewoldt et al (2008) for these relations). On the other hand, the real part of the Fourier transform $\hat{\tau}_r(\omega)$ corresponds to the out-of-phase component of the stress and the peaks at $\hat{\tau}_r(n\omega_d)$ are related to the viscous Chebyshev coefficients v_n. The spectral resolution of the data shown in figure 9 (d) is determined by the number of cycles recorded (5 cycles resulting in a resolution of $\Delta\omega = \omega_d/5$) while the maximum frequency component resolvable $\omega_{\max}$ is determined by the rate of sampling of the stress signal ($\omega_{\max} = \pi f = 188$ s^{-1} from a sampling rate of $f = 60$ Hz). The data however is only plotted up to $\omega/\omega_d = 11$ because the higher frequency components are primarily from background noise in the measured stress signal. The prominent peak for $\omega/\omega_d = 1$ and the very small magnitude of the higher harmonics in figure 9

(d) ($|\hat{\tau}_i(\omega)/\hat{\tau}_i(\omega_d)| < 0.005$ and $|\hat{\tau}_r(\omega)/\hat{\tau}_r(\omega_d)| < 0.005$ for $\omega \neq \omega_d$) reinforces the fact that for $\gamma_0 = 0.1$ the wormlike micellar fluid is within the linear regime of deformation.

3.4 Large Amplitude Regime - LAOS

Measurements of the form shown in section 3.3 illustrate the expected linear response of the CPyCl solution at small strain amplitudes ($\gamma_0 \ll 1$). In this section, the strain amplitude is increased to $\gamma_0 = 1$ (keeping the imposed frequency constant at $\omega_d = 0.63$ rad.s^{-1}) and the evolution in the velocity field within the fluid is measured. Figure 10 (a) shows the evolution of the velocity field within the fluid over one half period of oscillation. The profiles are plotted in the same manner as in figure 9 (a), i.e. every 20 frames and as averages over 20 frames. While this manner of plotting profiles does not technically show the true instantaneous velocity profile, the 20 frame averages were compared with single frame profiles and the two showed good agreement. Thus, error bars indicating the standard deviation of the velocity measurements (omitted in the plot) are typically the same size as the hollow symbols. At this larger strain amplitude, there is clear evidence of an inhomogenous banded flow with the velocity profile beginning to develop characteristics similar to those observed in figure 5 for steady shear flow at high shear rates. Due to the self-similarity of the velocity profiles observed during the oscillatory flow, each profile is fitted to the following functional form:

$$v(y) = V_w \left[s\left(\frac{y}{H}\right) + \frac{(1-s)}{2}\left(1 + \tanh\left(b\frac{(y-y_b)}{H}\right)\right)\right] \quad (3)$$

where y is the position across the gap, $y_b(t)$ is the position of the middle of the centrally located high shear rate band, and $b(t)$ is a measure of the band sharpness. For the case of large values of $b \gg 1$ (i.e. a sufficiently sharp band), $V_w(t)$ can be thought of as the velocity of the fluid at the upper wall at each point in time, and the parameter s can be thought of as a ratio of two shear rates, $\frac{\dot{\gamma}_0}{\dot{\gamma}_a}$, where $\dot{\gamma}_0$ is the "background" shear rate of the low shear rate regions near the top and bottom surfaces, and $\dot{\gamma}_a \equiv \frac{V_w}{H}$ is the apparent or nominal shear rate (V_w is the velocity at the wall and H is the gap height). This functional form has 4 parameters that are determined using a non-linear least squares minimization technique to fit each profile of figure 10 - these parameters are $V_w(t)$, $b(t)$, $y_b(t)$ and $s(t)$ (or $\dot{\gamma_0}(t)$). Figure 10 (a) shows an excellent agreement between the measured velocity values and the sigmoidal fit. The close fit to the functional form in equation 3 (a continuous function) suggests that the shear rate within the fluid varies continuously across the gap - this differs from observations made of banding under steady shear in Couette cells (see the work by Salmon et al (2003) or Ballesta et al (2007)), however the work by Britton and Callaghan (1997, 1999) did show that in cone-plate geometries, continuously varying shear rates were observed.

In addition to this spatially-banded structure, there is also good agreement between the measured velocity in the fluid adjacent to the top wall, and the oscillating velocity of the top plate, as seen in figure 10 (b). Once again, this indicates that there is no wall slip occuring at the top surface, and that the transparent film is effective at preventing slip for this particular oscillatory experiment.

Figure 10 (c) shows the Lissajous curve of the material stress-strain response for these particular oscillatory strain conditions. Qualitatively the curve looks very similar to that of figure 9 (c), however the larger values of the ratios $e_3/e_1 = 0.0175$ and $v_3/v_1 = 0.0359$ compared to the values for $\gamma_0 = 0.1$ indicate that the material is beginning to experience deformations in the non-linear regime. One interesting aspect of this set of data is how low the values of e_3/e_1 and v_3/v_1 are even though the material starts exhibiting a distinctly shear banded velocity profile. This suggests that for this particular fluid, relying on direct velocimetric measurements - and not on measurements of higher harmonics in the stress response - is a more sensitive probe of the onset of shear banding under LAOS.

In order to study any possible dynamic behavior of the shear bands, we tracked the middle position of the high shear rate band over one complete oscillation by plotting the value of the fitting parameter $y_b(t)$ (which corresponds to the location of the center of the high shear rate band) and the band sharpness $b(t)$ over the course of one period of oscillation. This data is shown in figure 11 and indicates that the values of y_b and b remain relatively constant over time. The center of the high shear rate band remains located near the middle of the sample at $\langle y_b \rangle = 0.8$ mm, while the value of $b(t)$ also remains constant with an average value of $\langle b \rangle = 3.78$. One interesting result is that the centrally located band is resolved for almost all points in time over the course of the oscillation. The only time period where the fitting technique cannot accurately locate the band is at the points of maximum strain (i.e. at the dashed vertical lines in figure 11). At these points the velocity within the fluid is almost zero everywhere (i.e. the imposed sinusoidal oscillation has reached maximum dis-

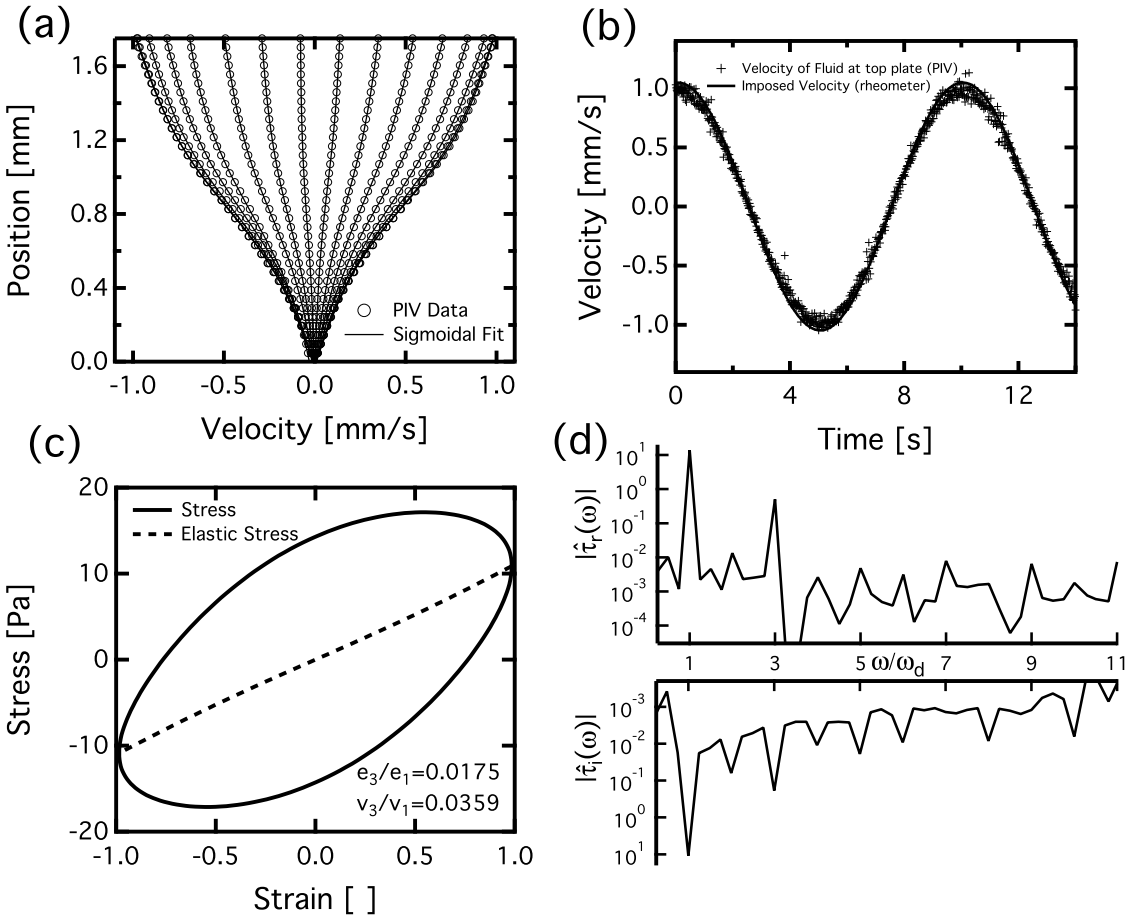

Fig. 10 Local and global rheological response within the CPyCl fluid under oscillatory shear with $\gamma_0 = 1$ and $\omega_d = 0.63$ rad.s^{-1} (De = 0.91, Wi = 0.91). Shear banded profiles are now clearly seen in (a), and are fit to the sigmoidal function of equation 3. The bulk response in (c) and power spectrum in (d) indicate that the material is beginning to exhibit nonlinear behavior.

placement) and so the fitting function of equation 3 is under-constrained.

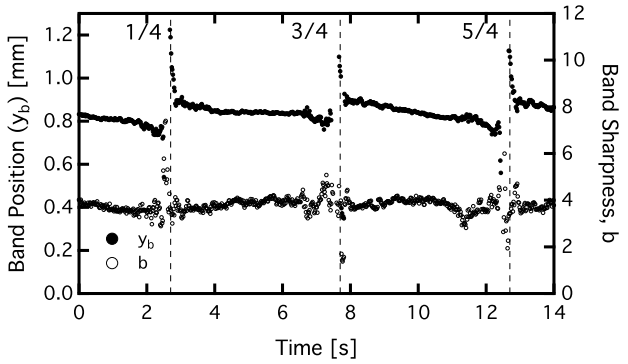

Fig. 11 Value of the fitting parameters y_b (band position) and b (band sharpness) during one period of oscillation ($T = 2\pi/\omega_d = 9.97$s) for the velocimetric data given in figure 10. Dashed vertical lines indicate times where the fluid has undergone 1/4, 3/4 and 5/4 of a period.

The LAOS behavior of the micellar fluid was also probed at an even larger strain amplitude $\gamma_0 = 3$, and once again local velocimetric data was compared with bulk measurements from the rheometer. Figure 12 (a) shows a more pronounced banding behavior in the set of velocity profiles measured during one half period. This data is also fit to the sigmoidal function described in equation 3 and the agreement between the fit and the measured data is again excellent. Figure 12 (b) again indicates that there is no observable wall slip occurring on the upper surface. The Lissajous curve presented in figure 12 (c) shows that the bulk stress-strain data measured in the fluid now exhibits a clearly nonlinear response. The values of e_3/e_1 and v_3/v_1 are now much larger than they were for the case in which γ_0=1. The positive value of e_3/e_1 can be attributed towards an intra-cycle strain stiffening in this material (Ewoldt et al, 2008, 2010). It is the appearance and growth of these higher harmonics that lead to the progressive deviation of the shear stress magnitude mea-

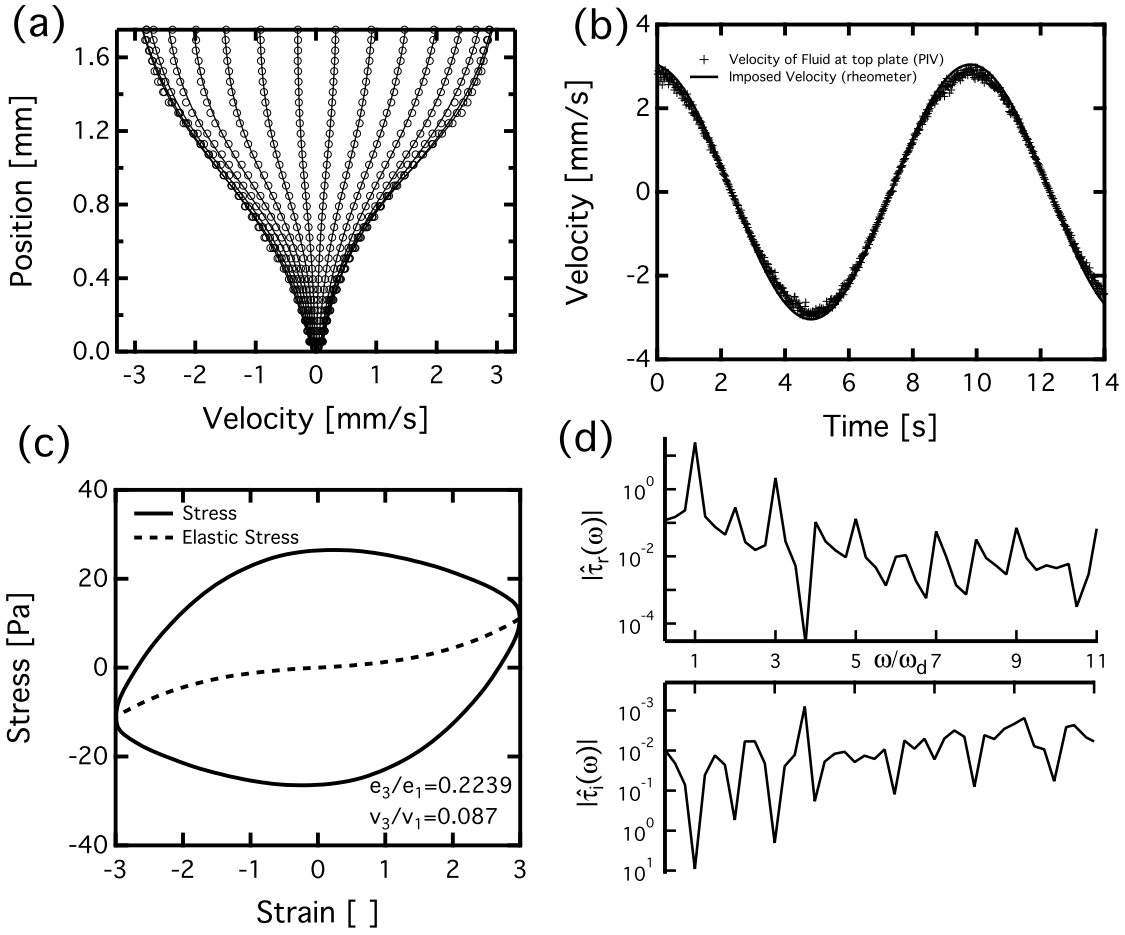

Fig. 12 Local and global rheological response within the CPyCl fluid under oscillatory shear with $\gamma_0 = 3$ and $\omega_d = 0.63$ rad.s^{-1} (De = 0.91, Wi = 2.73). The banded velocity profiles in (a) are now even more pronounced, and the Lissajous curve shown in (c) is clearly no longer elliptical, indicating that the material response is no longer linearly viscoelastic.

sured in steady and oscillatory shear and the failure of the Cox-Merz rule (see figure 1).

One interesting aspect of figure 12 (d) is the appearance of a more enhanced even harmonic at $\omega = 2\omega_d$ in the imaginary part of the discrete Fourier transform of the stress response. This suggests that there may be a small amount of wall slip occurring in the system (Hatzikiriakos and Dealy, 1991; Atalik and Keunings, 2004) however the fact that this harmonic is still relatively weak (a factor of 4 weaker than the intensity of the third harmonic at $\omega = 3\omega_d$) means that any wall slip that may be occurring is difficult to discern in figures 12 (a) and (b) and does not significantly affect the material response.

In figure 13 we plot the temporal evolution of the fitting parameters y_b and b for the velocimetric data shown in figure 12. For this case the average values $\langle y_b \rangle = 0.96$ mm and $\langle b \rangle = 4.30$ are larger than they were for the case in which $\gamma_0 = 1$ - this gives the appearance of a sharper band. The generally higher value of b agrees with what is observed under steady shear as the imposed shear rate is ramped up. Specifically, for the velocity profiles plotted in figure 5, as the value of $\dot{\gamma}$ is ramped up from 0.45 s^{-1} to 0.55 s^{-1} and 0.75 s^{-1} the fit of equation 3 to the velocity profiles yields values for b of 2.9, 3.2 and 3.7 respectively. Thus, more sharply banded profiles are observed at higher imposed shear rates in both oscillatory and steady shearing deformations.

The local temporal behavior of $y_b(t)$ and $b(t)$ indicates that there are more pronounced fluctuations occurring at this larger amplitude. However, the fluctuations in $y_b(t)$ are still small (on the order of 50 μm) and do not suggest that there is considerable intra or inter-cycle shift of the band position. A drift in the value of y_b of approximately 100 μm can be seen for 0 s $\leq t \leq$ 2 s and 10 s $\leq t \leq$ 12 s (before the sharp discontinuities at 2.2 and 12.2 seconds). However it is difficult to unambiguously determine the origin of this periodic fluctuation. One possible source of this drift

is slight irregularities in the air-sample interface which arise at points in the cycle when the sample has experienced maximum deformation. These irregularities distort the image, resulting in an apparent shift of the band position. An alternative source for these fluctuations is the type of dynamic band motion predicted in some theoretical studies (Zhou et al, 2010). These fluctuations might be expected to grow as the imposed strain amplitude is increased. However, with the current experimental setup, observing these dynamics at larger strain amplitudes is difficult due to even more pronounced interface irregularities.

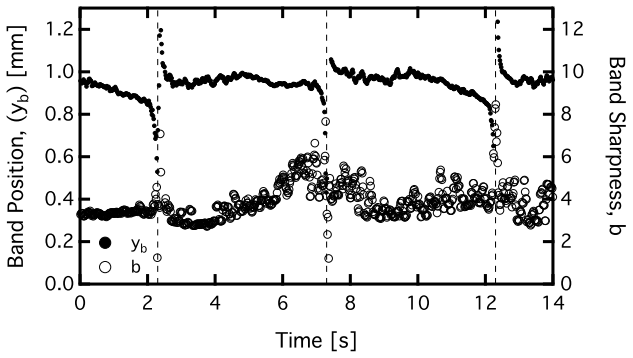

Fig. 13 Value of the fitting parameters y_b and b during one period ($T = 2\pi/\omega_d = 9.97$s) of oscillation for the velocimetric data given in figure 12.

While the data from this particular oscillatory test shows little variation in the value of y_b, equivalent Rheo-PIV tests done with the plano-concave lens result in profiles in which there is a sharper or narrower band near the midgap that moves vertically across the gap during the oscillation. Data and figures from these experiments are provided in the supporting materials. This difference, together with the contrast of the data shown in 5 (a-c) emphasizes the fact that the presence of the lens or a rigid outer boundary results in markedly different dynamic flow behavior in this shear-banding fluid. Based on these observations, the presence of the lens appears to result in generally less stable flow configurations for the CPyCl system under large amplitude oscillatory shear flow.

4 Conclusion

In this work, we have measured the local velocity fields within a wormlike micellar fluid (CPyCl:NaSal 100:60mM) under both steady and oscillatory shear using particle image velocimetry. We have also investigated the use of different experimental techniques that can be used to mitigate (a) wall slip effects that are endemic to Rheo-PIV experiments with complex fluids, and (b) some of the effects that edge irregularities in the cone-plate rheometer can have on the PIV measurements. Specifically, the use of a plano-concave optical lens placed at the geometry edge to improve image quality was discussed, and it was shown that the change in the boundary condition at the edge due to this rigid no-slip surface can result in a considerable qualitative change in the velocity profile observed within the fluid (both in oscillatory and steady shear). Additional flow visualization in the flow-vorticity plane was used to determine the critical shear rates beyond which secondary flows become substantial, and these imaging results were used to select test conditions for which there is minimal secondary flow occurring that might corrupt the PIV measurements.

Using the temporal and spatial resolution of the velocimetric measurement system, it has been possible to analyze the evolving velocity profiles within the fluid under oscillatory shear in the transition region as the fluid begins to experience large amplitude deformations and exhibits non-linear rheological behavior. The time periodic velocity field has been characterized for a CPyCl/NaSal micellar fluid under large amplitude oscillations and the velocity profiles exhibit a characteristic 3-banded structure that is well described by the sigmoidal function given in equation 3. The evolution of increasingly shear banded profiles is directly correlated with the bulk nonlinear response and pronounced shear banding is shown to occur even for small values of the nonlinearity indices e_3/e_1 and v_3/v_1. These results suggest that, at least for this particular class of wormlike micellar fluid, direct velocimetric measurements are a more sensitive method of determining onset of shear banding under LAOS, compared to measurements of higher harmonics in the bulk stress signal. For the strain amplitudes tested, the location of the shear band (quantified by the fitting parameter y_b) was shown to remain relatively constant over the oscillatory flow cycle. More detailed studies of dynamical changes in the interface position at progressively higher strain amplitudes will require additional advances in the Rheo-PIV technique to eliminate the impact of interfacial irregularities induced by fluid viscoelasticity on the imaging conditions.

The combination of localized velocimetric measurements and bulk rheological measurements provide detailed insight into the spatio-temporal dynamics of complex fluids under simple viscometric flows. By using LAOS as the imposed kinematic forcing we have been able to document the progressive evolution of the shear-banded structure and associated nonlinear rheological response in a model wormlike micelle solution. Such data can be

compared in the future with the predictions of rheological constitutive equations.

Acknowledgements The authors would like to thank M. A. Fardin for helpful discussions. L. Casanellas would also like to acknowledge the FPU-AP2008-03903 fellowship and the financial support from project nr. FIS2010-21924-C02-02 (MEC-Spain). TJO gratefully acknowledges support from the NSF Graduate Research Fellowship. Lastly the authors would like to thank Procter and Gamble for support of work on LAOS at MIT, and Chevron Energy Technology Corporation for supporting construction of the Rheo-PIV instrumentation at MIT.

References

Adams JM, Olmsted PD (2009) Nonmonotonic models are not necessary to obtain shear banding phenomena in entangled polymer solutions. Physical Review Letters 102(6), DOI 10.1103/PhysRevLett.102.067801

Adams JM, Fielding SM, Olmsted PD (2008) The interplay between boundary conditions and flow geometries in shear banding: Hysteresis, band configurations, and surface transitions. Journal of Non-Newtonian Fluid Mechanics 151(1-3):101 – 118, DOI 10.1016/j.jnnfm.2008.01.008, 4th Annual European Rheology Conference

Adrian RJ (1991) Particle-Imaging techniques for experimental fluid-mechanics. Annual Review of Fluid Mechanics 23:261–304

Adrian RJ (2005) Twenty years of particle image velocimetry. Experiments in Fluids 39:159–169, 10.1007/s00348-005-0991-7

Adrian RJ, Westerweel J (2011) Particle Image Velocimetry. Cambridge University Press

Atalik K, Keunings R (2004) On the occurrence of even harmonics in the shear stress response of viscoelastic fluids in large amplitude oscillatory shear. Journal of Non-Newtonian Fluid Mechanics 122(1-3):107 – 116, DOI 10.1016/j.jnnfm.2003.11.012

Ballesta P, Lettinga MP, Manneville S (2007) Superposition rheology of shear-banding wormlike micelles. Journal of Rheology 51(5):1047–1072, DOI 10.1122/1.2750665

Berret J, Roux D, Porte G (1994) Isotropic-to-nematic transition in wormlike micelles under shear. Journal De Physique II 4(8):1261–1279

Bird RB, Armstrong RC, Hassager O (1987) Dynamics of Polymeric Liquids Vol. 1, 2nd edn. John Wiley and Sons

Boukany PE, Wang SQ (2008) Use of particle-tracking velocimetry and flow birefringence to study nonlinear flow behavior of entangled wormlike micellar solution: From wall slip, bulk disentanglement to chain scission. Macromolecules 41(4):1455–1464, DOI 10.1021/ma702527s

Britton MM, Callaghan PT (1997) Two-phase shear band structures at uniform stress. Physical Review Letters 78(26):4930–4933, DOI 10.1103/PhysRevLett.78.4930

Britton MM, Callaghan PT (1999) Shear banding instability in wormlike micellar solutions. The European Physical Journal B - Condensed Matter and Complex Systems 7:237–249, 10.1007/s100510050610

Callaghan PT (2008) Rheo NMR and shear banding. Rheologica Acta 47:243–255, DOI 10.1007/s00397-007-0251-2

Cates ME, Fielding SM (2006) Rheology of giant micelles. Advances in Physics 55(7):799 – 879

Cho KS, Hyun K, Ahn KH, Lee SJ (2005) A geometrical interpretation of large amplitude oscillatory shear response. Journal of Rheology 49(3):747–758, DOI 10.1122/1.1895801

Davies CJ, Sederman AJ, Pipe CJ, McKinley GH, Gladden LF, Johns ML (2010) Rapid measurement of transient velocity evolution using GERVAIS. Journal of Magnetic Resonance 202(1):93 – 101, DOI 10.1016/j.jmr.2009.10.004

Dimitriou CJ, McKinley GH, Venkatesan R (2011) Rheo-PIV analysis of the yielding and flow of model waxy crude oils. Energy & Fuels 25(7):3040–3052, DOI 10.1021/ef2002348

Divoux T, Tamarii D, Barentin C, Manneville S (2010) Transient shear banding in a simple yield stress fluid. Physical Review Letters 104(20):208,301, DOI 10.1103/PhysRevLett.104.208301

Ewoldt RH, Hosoi AE, McKinley GH (2008) New measures for characterizing nonlinear viscoelasticity in large amplitude oscillatory shear. Journal of Rheology 52(6):1427–1458, DOI 10.1122/1.2970095

Ewoldt RH, Winter P, Maxey J, McKinley GH (2010) Large amplitude oscillatory shear of pseudoplastic and elastoviscoplastic materials. Rheological Acta 49(2):191–212, DOI 10.1007/s00397-009-0403-7

Fardin MA, Lasne B, Cardoso O, Grégoire G, Argentina M, Decruppe JP, Lerouge S (2009) Taylor-like vortices in shear-banding flow of giant micelles. Phys Rev Lett 103(2):028,302, DOI 10.1103/PhysRevLett.103.028302

Fardin MA, Lopez D, Croso J, Grégoire G, Cardoso O, McKinley GH, Lerouge S (2010) Elastic turbulence in shear banding wormlike micelles. Phys Rev Lett 104(17):178,303, DOI 10.1103/PhysRevLett.104.178303

Feindel K, Callaghan PT (2010) Anomalous shear banding: multidimensional dynamics under fluctuating slip conditions. Rheologica Acta 49:1003–1013,

10.1007/s00397-010-0470-9

Gibaud T, Barentin C, Manneville S (2008) Influence of boundary conditions on yielding in a soft glassy material. Physical Review Letters 101(25):258,302, DOI 10.1103/PhysRevLett.101.258302

Hatzikiriakos SG, Dealy J (1991) Wall slip of molten high-density polyethylenes 1. sliding plate rheometer studies. Journal of Rheology 35(4):497–523

Helgeson ME, Vasquez PA, Kaler EW, Wagner NJ (2009) Rheology and spatially resolved structure of cetyltrimethylammonium bromide wormlike micelles through the shear banding transition. Journal of Rheology 53(3):727–756, DOI 10.1122/1.3089579

Hu YT (2010) Steady-state shear banding in entangled polymers? Journal of Rheology 54(6):1307–1323, DOI 10.1122/1.3494134

Inn YW, Wissbrun KF, Denn MM (2005) Effect of edge fracture on constant torque rheometry of entangled polymer solutions. Macromolecules 38(22):9385–9388, DOI 10.1021/ma0510901

Keentok M, Xue S (1999) Edge fracture in cone-plate and parallel plate flows. Rheologica Acta 38(4):321–348

Läuger J, Stettin H (2010) Differences between stress and strain control in the non-linear behavior of complex fluids. Rheologica Acta 49:909–930, DOI 10.1007/s00397-010-0450-0

Lerouge S, Berret JF (2010) Shear-induced transitions and instabilities in surfactant wormlike micelles. In: Dusek K, Joanny JF (eds) Polymer Characterization, Advances in Polymer Science, vol 230, Springer Berlin / Heidelberg, pp 1–71

Lettinga MP, Manneville S (2009) Competition between shear banding and wall slip in wormlike micelles. Physical Review Letters 103(24):248,302, DOI 10.1103/PhysRevLett.103.248302

Lopez-Gonzalez MR, Holmes WM, Callaghan PT (2006) Rheo-NMR phenomena of wormlike micelles. Soft Matter 2:855–869, DOI 10.1039/B600978F

Manneville S (2008) Recent experimental probes of shear banding. Rheologica Acta 47:301–318, 10.1007/s00397-007-0246-z

Manneville S, Salmon JB, Bécu L, Colin A, Molino F (2004a) Inhomogeneous flows in sheared complex fluids. Rheologica Acta 43:408–416, 10.1007/s00397-004-0366-7

Manneville S, Salmon JB, Colin A (2004b) A spatio-temporal study of rheo-oscillations in a sheared lamellar phase using ultrasound. The European Physical Journal E: Soft Matter and Biological Physics 13:197–212, 10.1140/epje/e2004-00046-y

Manneville S, Bécu L, Grondin P, Colin A (2005) High-frequency ultrasonic imaging: A spatio-temporal approach of rheology. Colloids and Surfaces A: Physicochemical and Engineering Aspects 270-271:195 – 204, DOI 10.1016/j.colsurfa.2005.06.003, liquids and MesoScience

Marín-Santibáñez BM, Pérez-González J, de Vargas L, Rodríguez-González F, Huelsz G (2006) Rheometry-PIV of shear-thickening wormlike micelles. Langmuir 22(9):4015–4026, DOI 10.1021/la053167k, pMID: 16618140

Masselon C, Salmon JB, Colin A (2008) Nonlocal effects in flows of wormlike micellar solutions. Physical Review Letters 100(3):038,301

Masselon C, Colin A, Olmsted PD (2010) Influence of boundary conditions and confinement on nonlocal effects in flows of wormlike micellar systems. Phys Rev E 81(2):021,502, DOI 10.1103/PhysRevE.81.021502

McKinley GH, Öztekin A, Byars JA, Brown RA (1995) Self-similar spiral instabilities in elastic flows between a cone and a plate. Journal of Fluid Mechanics 285:123–164

Meeker SP, Bonnecaze RT, Cloitre M (2004a) Slip and flow in pastes of soft particles: Direct observation and rheology. Journal of Rheology 48(6):1295–1320, DOI 10.1122/1.1795171

Meeker SP, Bonnecaze RT, Cloitre M (2004b) Slip and flow in soft particle pastes. Phys Rev Lett 92(19):198,302, DOI 10.1103/PhysRevLett.92.198302

Mendez-Sanchez AF, Perez-Gonzalez J, de Vargas L, Castrejon-Pita JR, Castrejon-Pita AA, Huelsz G (2003) Particle image velocimetry of the unstable capillary flow of a micellar solution. Journal of Rheology 47(6):1455–1466, DOI 10.1122/1.1621421

Miller E, Rothstein JP (2007) Transient evolution of shear-banding wormlike micellar solutions. Journal of Non-Newtonian Fluid Mechanics 143(1):22 – 37, DOI DOI: 10.1016/j.jnnfm.2006.12.005

Møller PCF, Rodts S, Michels MAJ, Bonn D (2008) Shear banding and yield stress in soft glassy materials. Phys Rev E 77(4):041,507, DOI 10.1103/PhysRevE.77.041507

Nghe P, Degrè G, Tabeling P, Ajdari A (2008) High shear rheology of shear banding fluids in microchannels

Ober TJ, Soulages J, McKinley GH (2011) Spatially resolved quantitative rheo-optics of complex fluids in a microfluidic device. Journal of Rheology 55(5):1127–1159

Olmsted PD (2008) Perspectives on shear banding in complex fluids. Rheologica Acta 47:283–300, 10.1007/s00397-008-0260-9

Pipe CJ, Kim NJ, Vasquez PA, Cook LP, McKinley GH (2010) Wormlike micellar solutions: II. compar-

ison between experimental data and scission model predictions. Journal of Rheology 54(4):881–913, DOI 10.1122/1.3439729

Raffel M, Willert C, Wereley S, Kompenhans J (2007) Particle Image Velocimetry, A Practical Guide. Springer

Rehage H, Hoffmann H (1991) Viscoelastic surfactant solutions - model systems for rheological research. Molecular Physics 74(5):933–973

Salmon JB, Colin A, Manneville S, Molino F (2003) Velocity profiles in shear-banding wormlike micelles. Phys Rev Lett 90(22):228,303, DOI 10.1103/PhysRevLett.90.228303

Schmitt V, Lequeux F, Pousse A, Roux D (1994) Flow behavior and shear induced transition near an isotropic/nematic transition in equilibrium polymers. Langmuir 10(3):955–961, DOI 10.1021/la00015a057

Sui C, McKenna GB (2007) Instability of entangled polymers in cone and plate rheometry. Rheologica Acta 46(6):877–888, DOI 10.1007/s00397-007-0169-8

Tapadia P, Ravindranath S, Wang SQ (2006) Banding in entangled polymer fluids under oscillatory shearing. Physical Review Letters 96(19):196,001, DOI 10.1103/PhysRevLett.96.196001

Yesilata B, Clasen C, McKinley GH (2006) Nonlinear shear and extensional flow dynamics of wormlike surfactant solutions. Journal of Non-Newtonian Fluid Mechanics 133(2-3):73 – 90, DOI 10.1016/j.jnnfm.2005.10.009

Zhou L, Cook L, McKinley GH (2010) Probing shear-banding transitions of the VCM model for entangled wormlike micellar solutions using large amplitude oscillatory shear (LAOS) deformations. Journal of Non-Newtonian Fluid Mechanics 165(21-22):1462 – 1472, DOI 10.1016/j.jnnfm.2010.07.009